Progress in Natural Science: Materials International 29 (2019) 119–123

HOSTED BY

Contents lists available at ScienceDirect

Progress in Natural Science: Materials International

journal homepage: www.elsevier.com/locate/pnsmi

Crystal and electronic structure study of the $Li_2Mn_{1-x}Nd_xO_3$ battery cathode

Gültekin Çelik[a], Sevda Aktaş[a], Şule Ateş[a,*], O. Murat Özkendir[b], Wantana Klysubun[c]

[a] Selcuk University, Department of Physics, Faculty of Arts and Science, Campus, Konya, Turkey
[b] Tarsus University, Faculty of Technology, Energy Systems Engineering, Tarsus, Turkey
[c] Synchrotron Light Research Institute (SLRI), 111 University Avenue, Muang District, Nakhon Ratchasima 30000, Thailand

ARTICLE INFO

Keywords:
Cathode material
Crystal structure
Electronic structure
XAFS
Li-ion battery

ABSTRACT

Neodymium substituted Li_2MnO_3 samples were prepared by the solid-state reaction method. The crystal and electronic structure properties of the prepared samples were investigated by x-ray based techniques. According to the analysis, it was determined that Nd atoms did not sit in to the Cr coordinations in Nd substituted samples and built up a different crystal structure. To support the analysis of the crystal structure study of the samples, electronic structure properties of the Nd substituted samples were studied via the collected data by x-ray absorption fine structure (XAFS) spectroscopy from the Mn K-edge. The results of the data analysis revealed that due to the misfit with the ionic radii and also the oxidation states, substituted neodymium atoms built up isolated crystal domains in $Li_8Mn_5Nd_{18}O_{39}$ cubic crystal structure. The symmetry in Mn K-edge absorption data of the sample both in parent Li_2MnO_3 and Nd substituted samples confirmed that Mn coordinations has not been influenced by the Nd substitution.

1. Introduction

Since Li-ion batteries (LIBs) are the most interesting and promising systems for energy storage applications, and the ones have been widely studied and applied to electric vehicles, energy storage power stations and portable electronic devices such as cell phones, portable computers, digital cameras, etc. for the advantages of high energy density, high operating voltage, long life span, low cost and good safety. However, the energy density of current LIBs is still not enough because of the low capacities of the conventional LIB cathode materials, such as layered $LiCoO_2$ (130 mAh g^{-1}) [1] and olivine $LiFePO_4$ (163 mAh g^{-1}) [2]. It is known that the physical and chemical properties of cathode and anode materials are responsible for the electrochemical properties of LIBs [3–6]. Especially, cathode material affects substantially the performance and cost of a LIB. Since it typically has a lower specific capacity than the most common anode material, graphite (372 mAh g^{-1}), it is essential to develop high capacity cathode materials comparable to anode materials [7].

Extensive researches on the new cathode materials with high capacities are still one of the top studies for LIBs. Compared with the layered compounds based on cobalt or nickel oxides, lithium manganese oxide based compounds are cheaper, safer, more abundant and less toxic, and have attracted attention as one of the most promising cathode materials for future LIBs [8,9]. Moreover, they have the advantage of high reversible capacity (> 200 mAh g^{-1}) when charged above 4.5 V [8,10]. The one from these lithium manganese oxide cathode materials is Li_2MnO_3 having O^{3-} type layered and thermodynamically stable structure. Li_2MnO_3 like the other lithium manganese oxide compounds is electro active intercalation host material in lithium cells, too. Also, it has very high theoretical capacity and a particular electrochemical mechanism [11]. However, Li_2MnO_3 is known as electrochemically inactive below the usual cut-off charge potential of 4.5 V vs. Li/Li^+ [9]. Because of the atomic configurations in monoclinic Li_2MnO_3 (space group; *C*2/*m*:b1), where both manganese and lithium atoms occupy octahedral sites, it is difficult to oxidize Mn^{4+} to the Mn^{5+} state and more Li atom addition to this structure is not possible [9,12]. Thus, it is needed to investigate Li_2MnO_3 itself properties and its alternative element or compound doping structure due to all these advantages and disadvantages as the cathode material in the LIBs.

Li-rich Mn-based cathode materials have been widely studied for new generation Li-ion rechargeable batteries due to their high working voltage (3.5 V vs. Li/Li+), high specific capacity (250 mAh g^{-1}), large energy density (1000 Wh kg^{-1}), low cost, non-toxicity and several other advantages compared to the commercial other cathode materials [13–15]. Some studies for Li_2MnO_3 cathode materials have been reported in the literature. For example, Zuo et al. prepared a Mn-based Li-rich cathode material with a single-layer Li_2MnO_3 superstructure, which demonstrated a reversible capacity of ≈400 mAh g^{-1} with a

* Corresponding author.
E-mail address: suleates@gmail.com (Ş. Ateş).

https://doi.org/10.1016/j.pnsc.2019.03.010
Received 19 October 2018; Received in revised form 26 March 2019; Accepted 26 March 2019
Available online 10 April 2019
1002-0071/ © 2019 Chinese Materials Research Society. Published by Elsevier B.V. This is an open access article under the CC BY-NC-ND license (http://creativecommons.org/licenses/BY-NC-ND/4.0/).

stable discharge voltage and a high charge–discharge efficiency during cycling [16]. Xiang and Wu synthesized the pure and Al-doped Li_2MnO_3 materials, and claimed to have exhibited a great improvement on the rate capability and cycling stability compared to the Li_2MnO_3 sample of Al-doped Li_2MnO_3 sample [8]. Nanostructured (10–50 nm) cathode material Li_2MnO_3 was prepared via facile one-step hydrothermal process by Liu and Zhang. According to their report, the prepared materials exhibit a lower activation potential when being cycled, and delivered electrochemical performance between 4.3 V and 2.0 V at room temperature, with a capacity of 243 $mAh{\cdot}g^{-1}$ [9]. Yuzer and Ozkendir substituted Nd, Ce and Yb into the Li_2MnO_3 and investigated the crystal and electronic structure properties of these materials [12]. Li and Lei studied on nano-sized Li_2MnO_3 materials via the one-step solid state reaction method [11].

In this study, the crystal structure and electronic properties of the five different materials with the general formula $Li_2Mn_{1-x}Nd_xO_3$ (x = 0.00, 0.05, 0.10, 0.15, 0.20) are examined. To probe the influence of the *f* electrons on the Li_2MnO_3 crystal atoms, the studies were performed by the x-ray based techniques, such as x-ray diffraction (XRD), scanning electron microscopy (SEM) analyses, and x-ray absorption fine structure (XAFS) spectroscopy techniques.

2. Experimental

Neodymium (Nd) substituted Li_2MnO_3 cathode materials were synthesized by using Li_2O, MnO_2 and Nd_2O_3 powder compounds with high purity (> 99.99%) in the desired stoichiometric ratios as starting materials with the general formula $Li_2Mn_{1-x}Nd_xO_3$ (x = 0.05, 0.10, 0.15 and 0.20) by the solid-state reaction method.

The samples were prepared in several steps. The powders were mixed and milled for 6 h initially with RETSCH PM 100 at 200 rpm and all the milled samples were annealed in the furnace at 673 K (400 °C) for 6 h accordingly. 673 K was chosen because of the MnO_2 activity in the samples. MnO_2 powder may dissolve around 500 °C (with melting point at 535 °C) and can strongly interact with other elements. For the next step, mixed powders milled for 2 h and annealed up to 1023 K (750 °C) for 6 h in the furnace. As the last step, powders remilled for 2 h and annealed in the furnace at 1123 K (850 °C) for 12 h.

To study the crystal structure properties of the prepared cathode materials, such as crystal geometry, porosity, crystallite sizes, x-ray diffraction (XRD) measurements were taken using Bruker D8 Advance x-ray diffractometer with Cu Kα radiation (=1.54059 Å) at Selcuk University ILTEK (Advanced Technology Research & Application Center) laboratory in Konya, Turkey. The diffraction data was collected over the range of $10^\circ < 2\theta < 80^\circ$. SEM images for the morphologies of the samples were also taken at the ILTEK laboratory with Zeiss/EVO LS10 SEM imaging machine. The electronic structure of the samples was probed by using XAFS spectroscopy technique. XAFS data collection process was performed at the XAS beamline (Beamline-BL8:XAS) of the Siam Photon (SLRI) Synchrotron Radiation facility (Nakhon Ratchasima, Thailand) [17].

3. Results and discussion

XRD patterns for all samples are presented in Fig. 1. Fig. 1 shows that the substituted and non-substituted samples had partially or entirely similar reflection peaks. In XRD patterns belonging to all Nd-substituted samples the extra reflection peaks emerged. The sample with x = 0.0 had a uniform pattern as expected and highlighted a one-type crystal structure in the entire bulk. However, the XRD patterns for the other samples indicated a polycrystalline feature. According to Fig. 1, as the peak intensities belonging to Li_2MnO_3 crystal structure partially decreased with increasing Nd addition, ones belonging to $Li_8Mn_5Nd_{18}O_{39}$ crystal structure increased with Nd addition.

The detailed crystal structure analysis of the samples was achieved via a Rietveld method using MAUD software which was a diffraction/

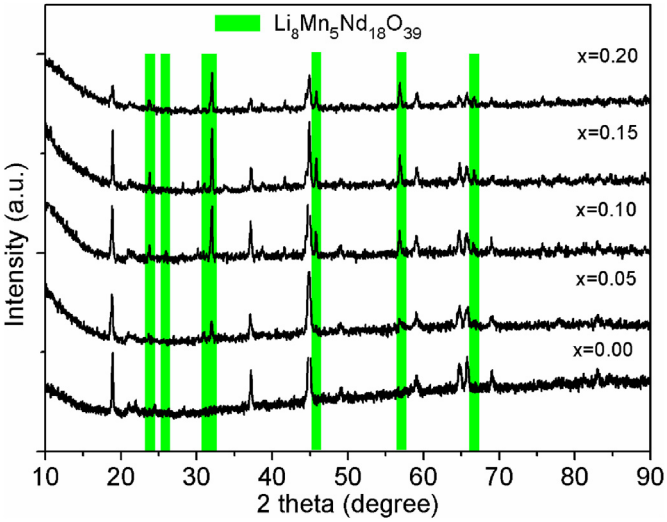


Fig. 1. XRD patterns of all Nd-substituted samples, in comparison.

reflectivity analysis code [18]. The analysis results are given in Table 1.

When Table 1 was examined, it is seen that the sample for x = 0.0 formed in only Li_2MnO_3 crystal structure and in a monoclinic geometry with a "*C*2/*c*:b1" space group in the bulk. However, the x = 0.05, 0.10, 0.15 and 0.20 substituted samples have multiplet peak structures, which addresses a polycrystalline feature. Two different crystal structures Li_2MnO_3 and $Li_8Mn_5Nd_{18}O_{39}$ were determined for these samples. Li_2MnO_3 had a monoclinic geometry with a "*C*2/*c*:b1" space group and, $Li_8Mn_5Nd_{18}O_{39}$ had a cubic geometry with a "*Pm*-3n" space group at different percentages.

The average crystallite sizes addressed the morphology of the pure and substituted samples were calculated via Scherrer's equation [19] given as:

$$A = K\lambda/(\beta \mathrm{Cos}\theta) \quad (1)$$

by using the taken XRD pattern data. In Eq. (1), *A* is the average crystallite size, *K* is the Scherrer constant (0.94), λ is the wavelength of the x-ray beam, *θ* is the Bragg angle and *β* is the full width at half maximum (FWHM) of the diffraction peak. According to the obtained results for all samples, the average crystallite size of Li_2MnO_3 and $Li_8Mn_5Nd_{18}O_{39}$ crystal structures were 21.5 nm and 34.92 nm, respectively.

In Fig. 2, SEM images are served for both pure and Nd-substituted Li_2MnO_3 samples. Looking at the SEM images, a general morphology having dominant small and sharp-edge attracts the attention. In the picture belonging to Li_2MnO_3 was observed a low porosity and smoother-edged structure. The sharper edged and porous structure of the particles increased as the contribution rate increased. It is obviously found that the changing substitution amounts caused change in the sample morphology. The increase or decrease in grain size with substitution amounts can be observed. It has been reported that the grain size decrease leads to the electrical conductivity increase in the literature [20–24]. Thus, the changing substitution amounts have the influence on their electrical properties. The substituted sample images including both Li_2MnO_3 and $Li_8Mn_5Nd_{18}O_{39}$ structures exhibited mixed smooth and sharp-edged small particles emphasizing polycrystalline structures. Therefore, we can say that the XRD patterns and SEM images of the samples are in agreement.

To study the electronic structure of the samples, x-ray absorption fine structure data were collected in transmission mode (TM) from Mn K-edge. The collected x-ray data for analysis was calibrated by adjusting the energy from a Mn foil. XAFS is one of the most useful element specific technique and an ideal tool for materials study [25]. The collected raw XAFS data of the samples were processed with the ATHENA

Table 1
Crystal structure analysis of the $Li_2Mn_{1-x}Nd_xO_3$samples.

Substitution ($Li_2Mn_{1-x}Nd_xO_3$)	Crystal	α	β	γ	a	b	c	Geometry	SG	%
0%	Li_2MnO_3	90	99.25004	90	4.89245	8.56131	9.50757	Monoclinic	*C*2/*c*:b1	100
5%	Li_2MnO_3	90	99.27276	90	4.89734	8.54723	9.54667	Monoclinic	*C*2/*c*:b1	96.50
	$Li_8Mn_5Nd_{18}O_{39}$	90	90	90	11.86385	11.86385	11.86385	cubic	*Pm*-3n	3.5
10%	Li_2MnO_3	90	99.24552	90	4.89715	8.57908	9.51862	Monoclinic	*C*2/*c*:b1	88.66
	$Li_8Mn_5Nd_{18}O_{39}$	90	90	90	11.87748	11.87748	11.87748	cubic	*Pm*-3n	11.34
15%	Li_2MnO_3	90	99.43304	90	4.89535	8.58649	9.49579	Monoclinic	*C*2/*c*:b1	84.86
	$Li_8Mn_5Nd_{18}O_{39}$	90	90	90	11.86241	11.86241	11.86241	cubic	*Pm*-3n	15.14
20%	Li_2MnO_3	90	100.03146	90	4.92571	8.49859	9.57595	Monoclinic	*C*2/*c*:b1	86.33
	$Li_8Mn_5Nd_{18}O_{39}$	90	90	90	11.86385	11.86385	11.86385	cubic	*Pm*-3n	13.67

and ARTEMIS codes to achieve best results [26]. The studied sample series have an important content with their electronic properties due to the rich molecular interplay among Li, Mn, O and Nd atoms.

Mn K-edge XAS spectra of the sample series are given in Fig. 3. The absorption spectra rised at 6530 eV and had a weak pre-edge peak at 6542 eV which appeared (assigned as "A") as a result of *1s-3d* quadrupole transition, where a dipole transition was forbidden, i.e., $\Delta l = \pm 1$.

The peak features on the Mn K-edge spectra had a high agreement with each other and a decrease at the normalized peak intensities was observed. The decrease in the peak intensities are related with the decrease in the Mn amounts. The agreement among the substituted and unsubstituted samples is a confirmation about the weak interaction of electronic levels of Nd with Mn valence or conduction bands. Besides, no energy shifts were observed at the peak symmetries in the spectra. The symmetry of the peak energies emphasizes the ionic stability of the manganese atoms in the sample environment. Besides, despite the neodymium substitution in the sample, the stability at the edge features of the manganese reflects an indirect interplay between Mn and Nd atoms via the oxygens. Beyond the pre-edge structure, a shoulder like a peak which is assigned as "B" emerges as a high energy levels (e_g) of Mn *dp* hybridized bands. This edge peak can be treated as the lower part of the main edge region and related with the low concentration of trivalent manganese atoms found in the sample. The peak energy of this edge was determined at 6551 eV. At 6560.6 eV, the main absorption edge of the tetravalent manganese atoms were determined as the final state for the 1s electrons dipole transition to unoccupied 4p levels. Heavy Nd atoms had unoccupied *f*-levels which do not support any

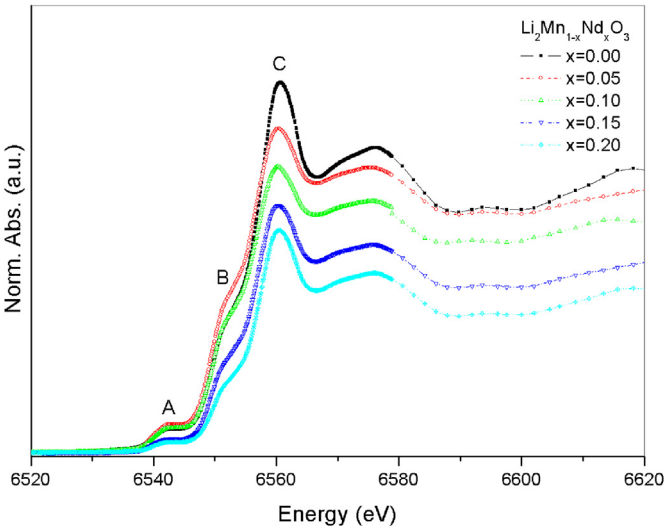
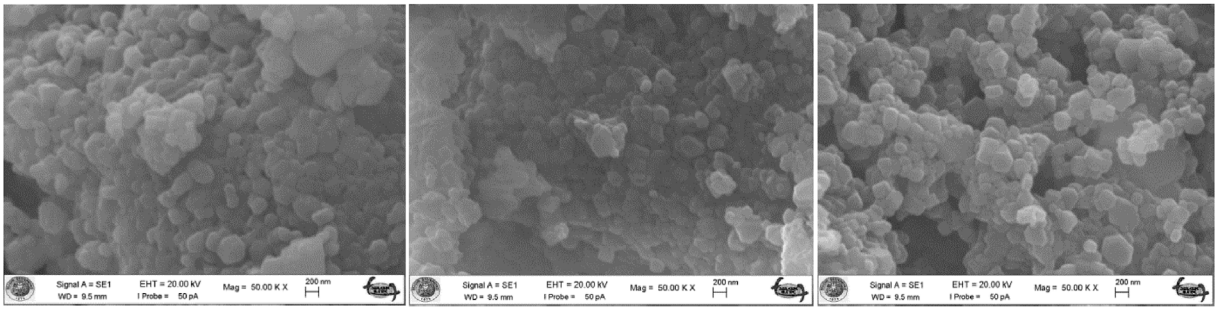
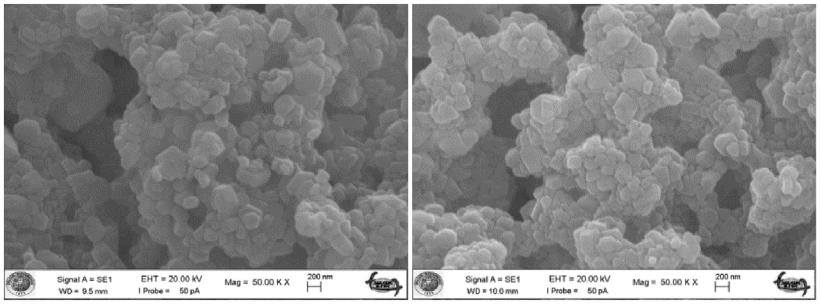


Fig. 3. Mn K-edge XAS spectra of the sample series.



a) Sample for x=0.0 b) Sample for x=0.05 c) Sample for x=0.10



d) Sample for x=0.15 e) Sample for x=0.20

Fig. 2. SEM images of the Nd-substituted samples. (a) x = 0.0, (b) x = 0.05, (c) x = 0.10, (d) x = 0.15, (e) x = 0.20.

coupling between outer shells of manganese which has *p*-levels due to the selection rules. So, Mn and Nd atoms tend to interact weakly with each other.

Beyond the main edge part (XANES) of the XAFS spectra, the EXAFS (Extended-XAFS) part (tail) lies. The strong and Gaussian shaped peak, which is assigned as "D", is due to the interference of the wave functions of the photoelectrons with the incoming x-rays produced in the mechanism of powerful scatterings from the nearest neighbors (i.e. oxygen). The tail of the XAFS spectra above the XANES region spectra is called as the EXAFS region and can be extracted to study on the environment of the source (Mn) atoms in the sample. The scattering intensity "chi" (χ) can be estimated from the collected EXAFS data as;

$$X = [\mu(E) - \mu_o(E)]/\Delta\mu_o \quad (2)$$

In the formula, μ is the absorption coefficient. With other experimental parameters, the formula giving the chi signal of the photoelectrons can also be estimated from; the EXAFS equation

$$X(k) = \sum [(N_j f_j(k) \bullet \exp(-2k^2\sigma_j^2))/(KR_j^2)]\sin[2kR_j + \delta_j(k)] \quad (3)$$

In this equation, N is the coordination number of the neighboring atom, $f_j(k)$ is the scattering amplitude, $\delta_j(k)$ is the scattering phase shift, R is the distance of the neighboring atom and σ_j^2 is the mean-square disorder with the neighboring atom distances.

The scattering data of the photoelectron can be used to study the local geometrical structures around the source atom, i.e. bond lengths, coordination numbers and the angles between atoms [27]. Besides, the periodicity of the oscillations in the region also allows us to determine the exact bond lengths and can provide information about the coordinations in the samples.

In Fig. 4, the scattering intensity (chi (χ)) spectra of the unsubstituted parent oxide cathode material (Li_2MnO_3) and 10% Nd substituted sample are given in comparison. The intensity of the scattering data is given with its k^2 power to make the influence of Nd original disturbances more obvious. In the figure, high scattering interactions takes place in the low k values, which has an opposite relation with the wavelength. In other words, the fatal scattering interactions occur at longer mean free paths. So, it is clear that, the Nd atoms are placed at distant locations and light atoms (Li, O) are placed in the region between Mn and Nd. The parent oxide sample scattering spectra has more smooth spectra than the substituted one. The multiple peak feature also reflects the inhomogeneous interstitial potentials formed by polycrystalline feature of the sample and presence of heavier atom in the crystal structure. The Fourier transform of the scattering intensity yields the radial distribution function (RDF), where the locations of the neighbor atoms are given on a one dimensional axis from the source atom.

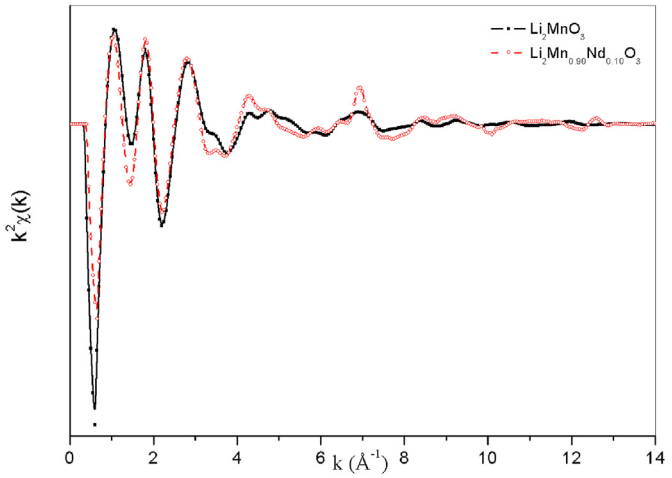


Fig. 4. Scattering intensity (chi (χ)) spectra of the unsubstituted parent oxide cathode material (Li_2MnO_3) and 10% Nd substituted sample.

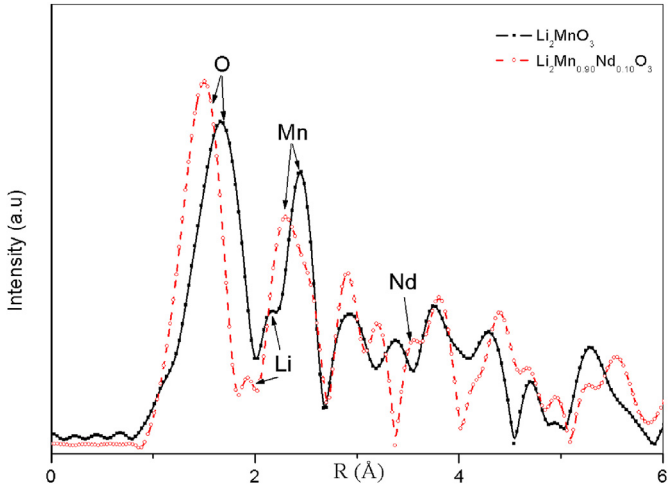


Fig. 5. RDF spectra comparison of the samples.

The RDF spectra comparisons of the samples are given in Fig. 5. The peaks contain information about atomic coordinations and their distances from the source atom. In case of closer atoms which have short distances to the source atom, but with different azimuthal or polar angles, their peaks overlap and may give broader peaks. So, fits on the RDF data should be performed by using the generated scattering paths by using the FEFF code, and the coordination numbers may be defined [27]. According to the analysis using path fits for Li_2MnO_3 parent oxide and $Li_8Mn_5Nd_{18}O_{39}$ sample, the first strong peaks are determined as the signals from the closest neighbors of manganese, oxygens, where six oxygen atoms sit in close distances to each other around 1.932 (± 0.02) Å. The second closest peak (weak) is from the two Li atoms which locate at about 2.827 Å distance from the Mn atom at the origin. The closest Mn atom is determined at a distance of 2.830 Å. For the Nd substituted samples, the closest Nd atom is determined to sit at a distance of 4.14 Å from the source Mn atom. The closest neighboring atoms are also pointed on the graph according to the atomic types.

4. Conclusions

The crystal structure and electronic properties of pure and Nd-doped materials with the general formula $Li_2Mn_{1-x}Nd_xO_3$ have been reported. As a results of analysis, while the sample for x = 0.0 forms in 100% Li_2MnO_3 crystal, the other samples (for x = 0.05, x = 0.10, x = 0.15, x = 0.20) form in two crystal phase in different ratios to be Li_2MnO_3 and $Li_8Mn_5Nd_{18}O_{39}$. Therefore it is believed that heavy Nd atoms didn't sit into Cr locations as expected. The electronic structure and influence of the Nd substitution into the Mn coordinations as well as its environment have been studied via the collected XAFS data from the Mn K-edge. The scattering intensities of the undoped (Li_2MnO_3) and 10% Nd doped samples show un-harmony at the high k-values, which denotes that low amount of different crystal formation is present in the substituted samples, i.e. $Li_8Mn_5Nd_{18}O_{39}$. Briefly, Nd atoms with larger atomic size and unmatched ionic properties of the neodymium atoms prefer to form different crystal structure and refuse to sit into the Mn coordinations. Besides, the change in the crystal properties appears in the radial distribution function of the samples with shifts at the atomic locations on the one dimensional axis.

Appendix A. Supplementary data

Supplementary data to this article can be found online at https://doi.org/10.1016/j.pnsc.2019.03.010.

References

[1] L. Xue, S.V. Savilov, V.V. Lunin, H. Xia, Adv. Funct. Mater. 28 (2018) 1705836.
[2] C. Zhao, L. Wang, H. Wu, J. Chen, M. Gao, Mater. Res. Bull. 97 (2018) 195.
[3] K. Wu, K. Du, G. Hu, J. Mater. Chem. A 6 (2018) 1057.
[4] K. Wu, D. Liu, Y. Tang, Electrochim. Acta 263 (2018) 515.
[5] P.C. Lian, X.F. Zhu, S.Z. Liang, Z. Li, W.S. Yang, H.H. Wang, Electrochim. Acta 55 (2010) 3909.
[6] Y. Ren, L.J. Hardwick, P.G. Bruce, Angew. Chem. Int. Ed. 49 (2010) 2570.
[7] S. Goriparti, E. Miele, F. De Angelis, E. Di Fabrizio, R.P. Zaccaria, C. Capiglia, J. Power Sources 257 (2014) 421e443.
[8] Y. Xiang, X. Wu, Ionics 24 (2018) 83.
[9] G. Liu, S. Zhang, Int. J. Electrochem. Sci. 11 (2016) 5545.
[10] H. Yu, H. Zhou, J. Phys. Chem. Lett. 4 (2013) 1268.
[11] S. Li, D. Lei, AIP Conf. Proc. 1890 (2017) 040037, , https://doi.org/10.1063/1.5005239.
[12] A. Yuzer, O.M. Ozkendir, J. Electron. Mater. 45 (2016) 2.
[13] J. Wang, H. Wu, Y. Cui, S. Liu, X. Tian, Y. Cui, X. Liu, Y. Yang, ACS Appl. Mater. Interfaces 10 (2018) 5125.
[14] T. Matsunaga, H. Komatsu, K. Shimoda, T. Minato, M. Yonemura, T. Kamiyama, S. Kobayashi, T. Kato, T. Hirayama, Y. Ikuhara, H. Arai, Y. Ukyo, Y. Uchimoto, Z. Ogumi, J. Phys. Chem. Lett. 7 (2016) 2063.
[15] H.J. Lee, S.B. Lim, J.Y. Kim, M. Jeong, Y.J. Park, W.S. Yoon, ACS Appl. Mater. Interfaces 10 (2018) 10804.
[16] Y. Zuo, B. Li, N. Jiang, W. Chu, H. Zhang, R. Zou, D. Xia, Adv. Mater. 30 (2018) 1707255.
[17] W. Klysubun, P. Sombunchoo, N. Wongprachanukul, P. Tarawarakarn, S. Klinkhieo, J. Chaiprapa, P. Songsiriritthigu, Nucl. Instrum. Methods Phys. Res. 582 (2007) 87.
[18] L. Lutterotti, D. Chateigner, S. Ferrari, J. Ricote, Thin Solid Films 450 (2004) 34.
[19] H.O. Abd-Alkader, N.M. Dearz, Int. J. Electrochem. Sci. 8 (2013) 8614.
[20] R. Hariharan, P. Gopalan, J. Mater. Res. 27 (2012) 2017.
[21] E.T. Wefring, F.H. Schader, K.G. Webber, M.A. Einarsrud, T. Grande, J. Eur. Ceram. Soc. 36 (2016) 497.
[22] M.I. Mohammed, A.A. Elbadawi, H.H. Abuellhassan, J. Appl. Ind. Sci. 1 (2013) 12.
[23] T. Šalkus, E. Kazakevičius, J. Banys, M. Kranjčec, A.A. Chomolyak, Yu.Yu. Neimet, I.P. Studenyak, Solid State Ionics 262 (2014) 597.
[24] W. Luo, L. Zhu, X.J. Zheng, Chin. Phys. Lett. 26 (2009) 117502.
[25] M. Balasubramanian, J. McBreen, NSLS Activity Report vol. 2, (2001), p. 10.
[26] B. Ravel, J. Synchrotron Radiat. 8 (2001) 314.
[27] A.L. Ankudinov, B. Ravel, J.J. Rehr, S.D. Conradson, Phys. Rev. B 56 (1997) R1712.